Microfluid Nanofluid (2007) 3:347–358
DOI 10.1007/s10404-006-0129-0

RESEARCH PAPER

# Experiment and simulation of mixed flows in a trapezoidal microchannel

**Keisuke Horiuchi · Prashanta Dutta · Cecilia D. Richards**

Received: 19 August 2006 / Accepted: 6 October 2006 / Published online: 30 November 2006


**Abstract** This paper presents experimental and numerical results of mixed electroosmotic and pressure driven flows in a trapezoidal shaped microchannel. A micro particle image velocimetry ($\mu$PIV) technique is utilized to acquire velocity profiles across the microchannel for pressure, electroosmotic and mixed electroosmotic-pressure driven flows. In mixed flow studies, both favorable and adverse pressure gradient cases are considered. Flow results obtained from the $\mu$PIV technique are compared with 3D numerical predictions, and an excellent agreement is obtained between them. In the numerical technique, the electric double layer is not resolved to avoid expensive computation, rather a slip velocity is assigned at the channel surface based on the electric field and electroosmotic mobility. This study shows that a trapezoidal microchannel provides a tapered-cosine velocity profile if there is any pressure gradient in the flow direction. This result is significantly different from that observed in rectangular microchannels. Our experimental results verify that velocity distribution in mixed flow can be decomposed into pressure and electroosmotic driven components.

**Keywords** Trapezoidal microchannel · Microfluidics · Electroosmotic flow · $\mu$PIV · Mobility

K. Horiuchi · P. Dutta (✉) · C. D. Richards
Mechanical and Materials Engineering,
Washington State University,
Pullman, WA 99164-2920, USA
e-mail: dutta@mail.wsu.edu

*Present Address:*
K. Horiuchi
Mechanical Engineering Research Lab, Hitachi Ltd,
Ibaraki, Japan

## 1 Introduction

In the past two decades, microchannels have attracted increasing attention in ''lab-on-a-chip'' devices. Unlike capillaries, microchannels can be formed to build complicated geometries. Commonly used microchannel fabrication techniques are physical etching, chemical etching, soft lithography or a combination of them. Among them, soft lithography is the most successful technology for the formation of complex microchannels in polymeric materials, due to its potential advantages such as flexibility, reproducibility, reliability, simplicity, and cost-effectiveness (Xia and Whitesides 1998). In soft lithography, microchannels are fabricated through replica molding of a polymeric material after patterning positive relief on a substrate using photolithography. Depending on the type of photoresist used in the photolithography process, the resultant microchannel may not have a perfect rectangular shape in cross section. Figure 1 shows the profile of two microchannels (Channel 1, 300 μm base and Channel 2, 140 μm base) fabricated on polydimethyl siloxane (PDMS) using soft lithography, where AZP4620 (AZ Electronic Materials, NJ, USA) is used as photoresist. Neither channel has a sharp edge due to an imperfect developing process. As a matter of fact, for small aspect (depth to width) ratio channels, a trapezoidal cross section is more likely to be seen rather than a perfect rectangular profile if the soft lithography technique is applied. Isotropic etching also results in a non-rectangular shaped microchannel due to the under-cutting of the mask used in the etching process. Dutta and Leighton (2001) presented a theoretical study on dispersion in a rectangular microchannel bounded by two quarter-circular disks.

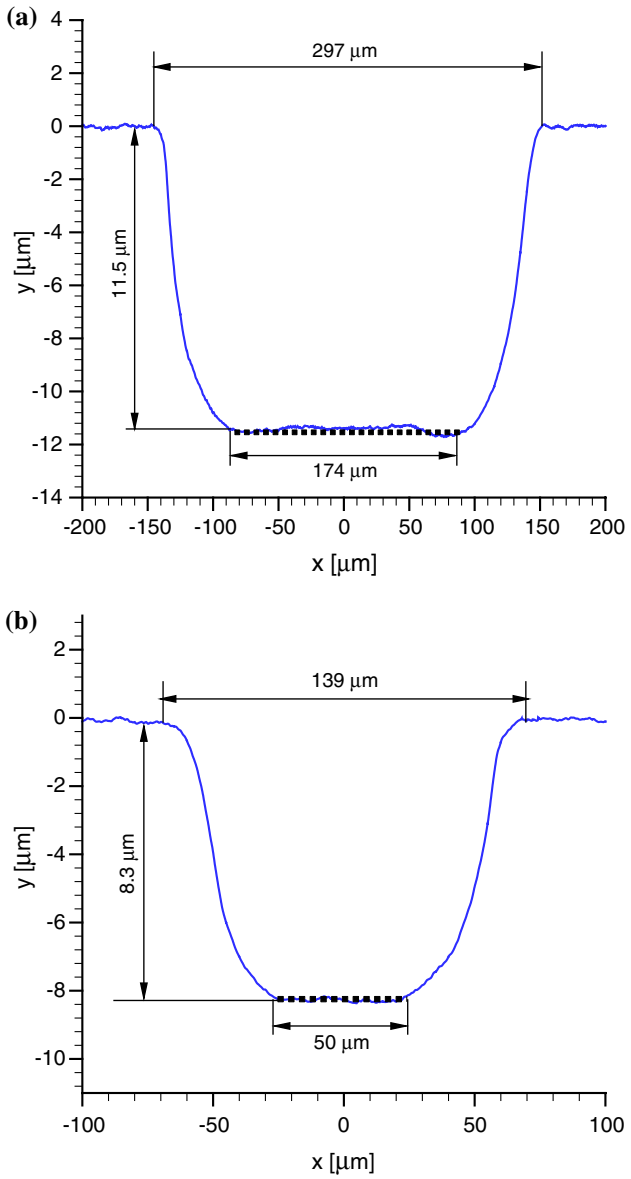


**Fig. 1** Profiles of microchannel fabricated using soft lithography technique. Measurements were done by a profilometer (SPN Technology, Inc., CA). **a** Channel 1, 300 µm base and **b** Channel 2, 140 µm base. The *dotted line* shows the base of the channel

Flow studies in microchannels have been reported by several research groups. Liquid flow visualization techniques in microgeometries can be divided into scalar-based and particle-based methods. There exist a number of scalar image velocimetry (SIV) methods such as laser-induced fluorescence (Erickson et al. 2003), molecular tagging velocimetry (Maynes and Webb 2002), photo-bleached fluorescence (Paul et al. 1998) and microbubble lensing-induced photobleaching (Sinton et al. 2003). In SIV, the velocity profile is quantified by tracing transported dye (normally fluorescent or phosphorescent). However, this technique suffers from serious limitations if the flow is not steady and fully developed. For quantification of the velocity distribution across a microgeometry, particle based methods are appropriate. Although laser Doppler velocimetry (Tieu et al. 1995) and particle tracking velocimetry (PTV) (Devasenathipathy et al. 2002) are available at the micro scale, particle image velocimetry (PIV) is the most common particle based flow analysis technique. This is primarily due to the ability of PIV to acquire velocity distributions with high spatial resolution and accuracy. The first work in which PIV was applied to the micro scale was presented by Santiago et al. (1998). They utilized a continuous mercury arc lamp, so their system was suitable for slow motion of photosensitive biological molecules. Meinhart et al. (1999) introduced a pulsed laser as the light source to effectively freeze the motion of seeding particles, and thus extended the measured velocity range. This group also introduced an algorithm to reduce the effects of the Brownian motion of seeding particles by averaging in correlation space over multiple image pairs (Meinhart et al. 2000a). In last couple of years, a number of research groups contributed to the understanding of the depth of focus (Olsen and Adrian 2000; Wereley et al. 2002; Bourdon et al. 2004), and developed high resolution $\mu$PIV systems (Keane et al. 1995; Takehara et al. 2000). Cummings et al. (2000) first visualized electrokinetic flows using a $\mu$PIV technique. Later on, Kim et al. (2002) presented both experimental and numerical work in a grooved microchannel. In all these experimental studies either pressure or electrokinetic driven flow was obtained in a rectangular microchannel, and none of them considered trapezoidal shape geometry. Moreover, no previous experimental work has addressed mixed electroosmotic and pressure driven flow in microgeometries both numerically and experimentally.

In this study, we have developed a $\mu$PIV system from an existing macro scale PIV tool to quantify the velocity distribution in trapezoidal microchannels. Here an external pressure is imposed on an electroosmotically driven mechanism to study the combined flow phenomena. This paper is arranged as follows. In next section, theory and governing equations for electrokinetic microflow are provided. This is followed by the numerical scheme and its validation. Next the fabrication techniques and $\mu$PIV setup developed for this study are discussed. Results of electrophoretic, pressure, electroosmotic and mixed electroosmotic-pressure driven flow velocities are then provided. Finally discussion and conclusions of this experimental work are presented.

## 2 Electroosmotic flow

Electroosmotic flow is the bulk motion of an electrolyte solution under the action of an electric field (Yang and Li 1998). The governing equations for ionized incompressible flows with electrokinetic body forces are given by the modified Navier–Stokes equations (Probstein 1994):

$$\rho_f\left(\frac{\partial \vec{V}}{\partial t}+\left(\vec{V}\cdot\nabla\right)\vec{V}\right)=-\nabla P+\mu\nabla^2\vec{V}+\rho_e\vec{E} \qquad (1)$$

where $\rho_f$ is fluid density, $t$ time, $\vec{V}=(u,v,w)$ divergence free velocity field $\left(\nabla\cdot\vec{V}=0\right)$, $P$ is pressure, $\mu$ viscosity, and $\rho_e$ net electric charge density. The externally applied electric field, $\vec{E}=-\nabla\varphi$, is governed by the charge conservation equation

$$\nabla\cdot[\sigma\nabla\varphi]=0 \qquad (2)$$

where $\phi$ is externally applied electric potential and $\sigma$ fluid conductivity. The electrokinetic potential distribution ($\psi$ ) due to the presence of the electric double layer (EDL) is related to the electric charge density ($\rho_e$ ) by the Poisson–Boltzmann equation (Probstein 1994)

$$\nabla^2\psi=-\frac{\rho_e}{\varepsilon}=-\frac{e(n^+z^++n^-z^-)}{\varepsilon} \qquad (3)$$

where $e$ is electron charge, $\varepsilon$ permittivity, $z$ valence, and $n$ ion number concentration. For a symmetric, dilute and univalent electrolyte ($z^+ = -\ z^- = z$ ), the charge density can be expressed as (Dutta and Beskok 2001)

$$\rho_e=-2\,e\,z\,n_0\sinh\left(\frac{ez\psi}{k_BT}\right) \qquad (4)$$

where $k_B$ is Boltzmann constant, $T$ absolute temperature, and $n_o$ ion number concentration in the bulk solution.

The main simplifying assumptions used to obtain the above equations are:

(a) The fluid is Newtonian, and the microflow is laminar.
(b) Fluid properties such as, viscosity, permittivity, and conductivity are independent of local and overall electric field strength.
(c) Temperature variation due to Joule heating is negligible. Hence fluid properties are assumed constant.
(d) Ions are point charges, and ionic diffusion effects are much higher than ionic convection.
(e) The solvent is continuum.
(f) In the charge conservation equation, the effects of advection and diffusion are negligible.

## 3 Numerical scheme and validation

The electrokinetic velocity field can be obtained by solving Eqs. (1–3) with appropriate boundary conditions. However, the direct solution of the coupled system will be extremely (computationally) expensive, especially for a 3D geometry, due to the different length scales associated with microfluidic devices. Generally microfluidic channels are 1–10 microns thick, 10–500 microns wide, and 1–5 cm long. In addition to the diverse spatial length scales, the EDL thickness ranges between 1 and 10 nm. The complete solution of 3D electrokinetic flows is presented analytically (Yang and Li 1998) and numerically (Patankar and Hu 1998) based on the Debye–Huckel approximation. Dutta et al. (2002) presented the steady solutions for electroosmotic and mixed flows in planar geometries for different values of ionic charge parameter using a spectral element method.

The computational effort required for 3D electrokinetic flow can be minimized considerably by placing an effective slip velocity at the channel wall to capture the thin EDL effects on the fluid flow. The slip velocity concept has been reported recently in a number of numerical works to study electroosmotic flow in planar and arbitrary geometries (Hlushkou et al. 2005 and references therein).

In this study, a 3D finite volume scheme is used to solve the Navier–Stokes equations without any electrokinetic body forces. To model the electrokinetic effects in electroosmotic and mixed flow, the velocity at the slip plane is specified as

$$\vec{V}=-\left(\frac{\varepsilon\zeta\nabla\phi}{\mu}\right)=-M_{eo}\nabla\phi \qquad (5)$$

where $\zeta$ is zeta potential and $M_{eo}$ electroosmotic mobility. For simplicity electroosmotic mobility is assumed constant along the channel wall, and it has been obtained from the experiments. In solving the pure electroosmotic velocity field, the pressure is maintained atmospheric at both inlet and exit reservoirs. The external electric field distribution is obtained from Eq. (2), which is subjected to insulating boundary conditions ($\nabla\phi\cdot\vec{n}=0$) on the channel surfaces.

A semi implicit method for pressure linked equations revised (SIMPLER) algorithm in a staggered grid system has been used to solve the velocity field (Patankar 1980). A line by line method is employed to solve each dependent variable, where each partial differential equation is discretized as algebraic equations along each grid line, and a tri-diagonal matrix algorithm (TDMA) is used to solve them directly.

Figure 2 shows the numerical results for pressure driven flows in rectangular microchannels with a pressure gradient of 9,319 N/m$^3$. The flow velocity becomes fully developed within 2 mm from the upstream reservoir. The stream-wise velocity distribution presented here is averaged in the depth-wise direction, and is extracted from the fully-developed region (1 cm away from the entrance). Two different channel sizes are considered in this numerical work: (a) 300 × 12 μm and (b) 140 × 8 μm. For the same pressure gradient, a thinner channel yields a lower flow velocity. These numerical results are also compared with analytical results of Ebadian and Dong (1998), and as shown in the Fig. 2 an excellent agreement is obtained throughout the computational domain.

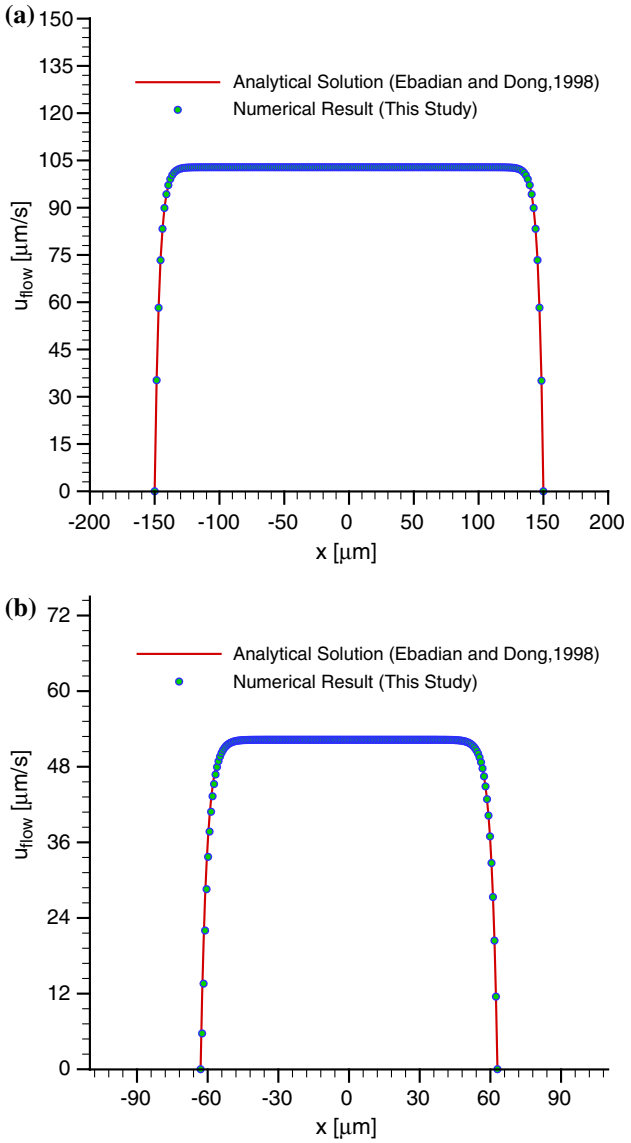


**Fig. 2** Validation of numerical results for pressure driven flows ($dP/dx = -9{,}319$ N/m$^3$) in rectangular microchannel. **a** 300 × 12 μm and **b** 140 × 8 μm microchannels. A 3D finite volume scheme is used to simulate flow in microchannels. Analytical solution of pressure driven flow in rectangular channel by Ebadian and Dong (1998) is used for validation

## 4 Experimental

### 4.1 Microfabrication technique

In this study, two different kinds of microchannels (PDMS–glass and PDMS–PDMS) are fabricated. Both PDMS and glass materials are favorable to electrokinetic flow, are compatible with a variety of bio-analytical processes, and are suitable for optical based detection techniques. Here microchannel structures are formed in PDMS using soft lithography technique (Xia and Whitesides 1998).

Figure 3 illustrates the procedures used to form a trapezoidal microchannel with embedded electrodes. First, a positive photoresist (AZP4620, AZ Electronic Materials, NJ, USA) is spin coated on a silicon wafer at 2,000 rpm for 19 s to form a 10 μm thick layer. After 60 s of ultraviolet (UV) light exposure, a patterned positive relief is prepared by dissolving the exposed regions with the corresponding developer (AZ400, AZ Electronic Materials, NJ). Meanwhile, the PDMS prepolymer and the curing agent (Sylgard 184, Dow Corning Inc., MI, USA) are mixed at a ratio of 10:1. The mixed liquid elastomer is then degassed for 2 h at 0.001 Torr and cast onto the prepared substrate after placing capillaries on the inlet and outlet reservoir positions. After curing for 6 h at 80°C in a hot oven, the solidified PDMS is carefully peeled off and capillaries are removed to reveal holes in the PDMS. The resultant slab is the top layer of the microchannel. For a PDMS–glass microchannel, a cover glass is used as the bottom layer, while for the PDMS–PDMS channel another layer of thin flat PDMS is formed.

Next, to form the electrodes, 5 nm of titanium tungsten (TiW) is sputtered on the bottom layer followed by 95 nm of gold (Au). Here, TiW is deposited as a binding agent since the bonding strength between Au and glass/PDMS is very weak. In order to minimize flow disturbances, the total electrode thickness is re-

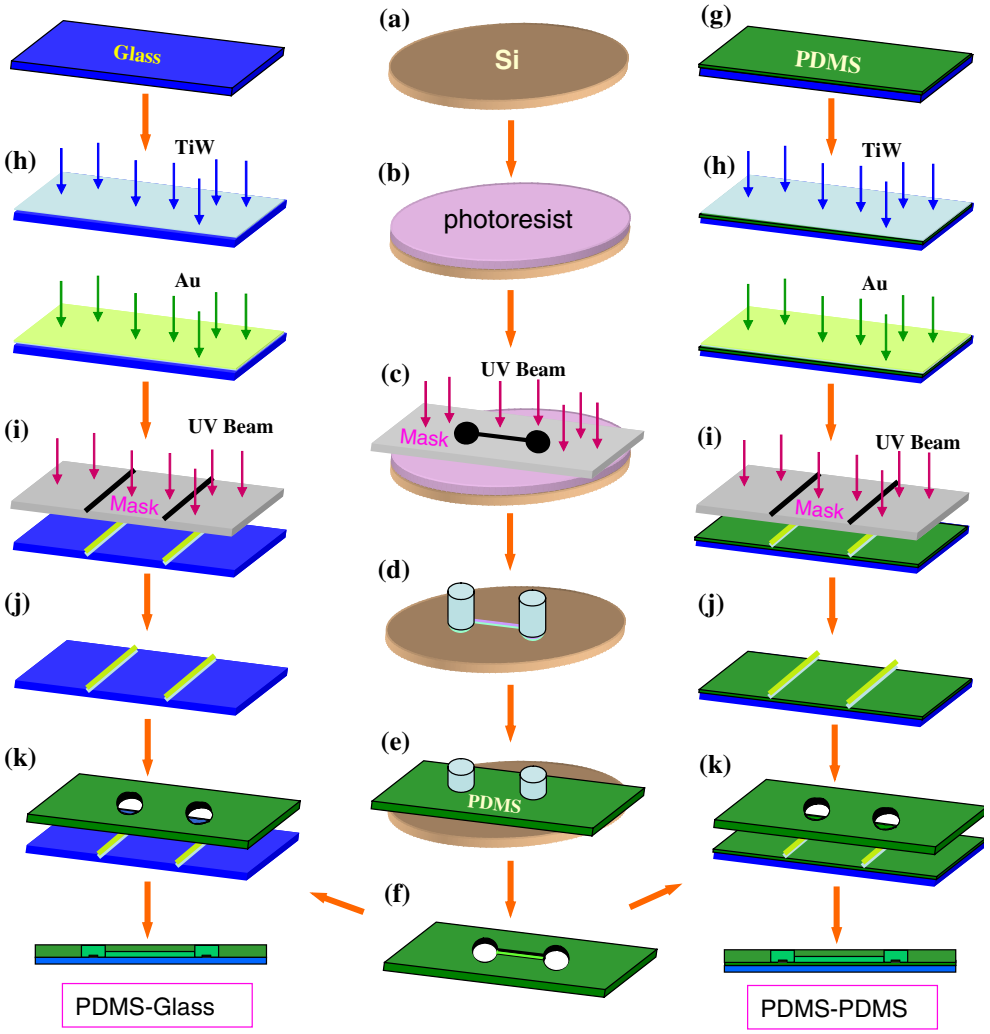


**Fig. 3** Fabrication schemes used to form PDMS–glass and PDMS–PDMS microchannels. **a** Substrate cleaning, **b** photoresist spin coating, **c** UV exposure, **d** photoresist development and capillary placement, **e** PDMS casting, **f** top layer, **g** PDMS spin coating and curing, **h** TiW and Au sputtering, **i** patterning of electrodes, **j** bottom layer, and **k** bonding. Titanium tungsten and Au electrodes are deposited to apply electric fields in electrokinetic flows

stricted to 100 nm. The precise patterning of photoresist (AZ4620) on this thin metal layer is carried out by identical photolithography used to prepare the top layer. Gold uncoated by photoresist is etched, rinsed in DI water, and then agitated in 30% hydrogen peroxide for 40 s to remove the TiW layer. Cleaning with acetone and IPA washes away photoresist, so a patterned Au–TiW layer is formed on the bottom layer. Oxygen RF plasma etching (PDC-32G, Harrick Scientific Co., NY, USA) is utilized for 20 s to temporally activate the PDMS surface before bonding the two layers.

### 4.2 Micro particle image velocimetry system

An in-house $\mu$PIV system has been developed from an existing regular-PIV system. Figure 4 shows the schematic of the microscale PIV system used in the experimental work. It consists of a Nd:YAG laser, a CCD camera, optical components (neutral density filter, beam expander, dichroic mirror, color filters, and objective lens), a synchronizer, and a data acquisition system. Here a 7 ns pulsed laser is used to illuminate the seeding particles in the microchannel. For this $\mu$PIV setup, the intensity of the laser (Nd:YAG Powerlite, Continuum, CA, USA) is reduced to 10 mJ by using a neutral density filter (FSR-OD80, Newport Corp, CA, USA). A Galilean type beam expander, composed of two lenses (01LPK007/078 and 01LAO256/078, Melles Griot, CA, USA), is placed to expand and collimate light beams into the inverted fluorescent microscope (CKX41, Olympus Co., Tokyo, Japan). The expanded beam is then reflected by the dichroic mirror and illuminates the seeding particles in the microchannel test section. In this study, 500 nm orange fluorescent (540 nm excitation and 560 nm emission) polystyrene microspheres (Molecular Probes, OR, USA) are used as seeding particles. Since the orange fluorescent seeding particles have a very narrow wavelength difference between excitation and emission, a special dichroic cube (Z532/10, 532RDC, HQ575/50) is installed

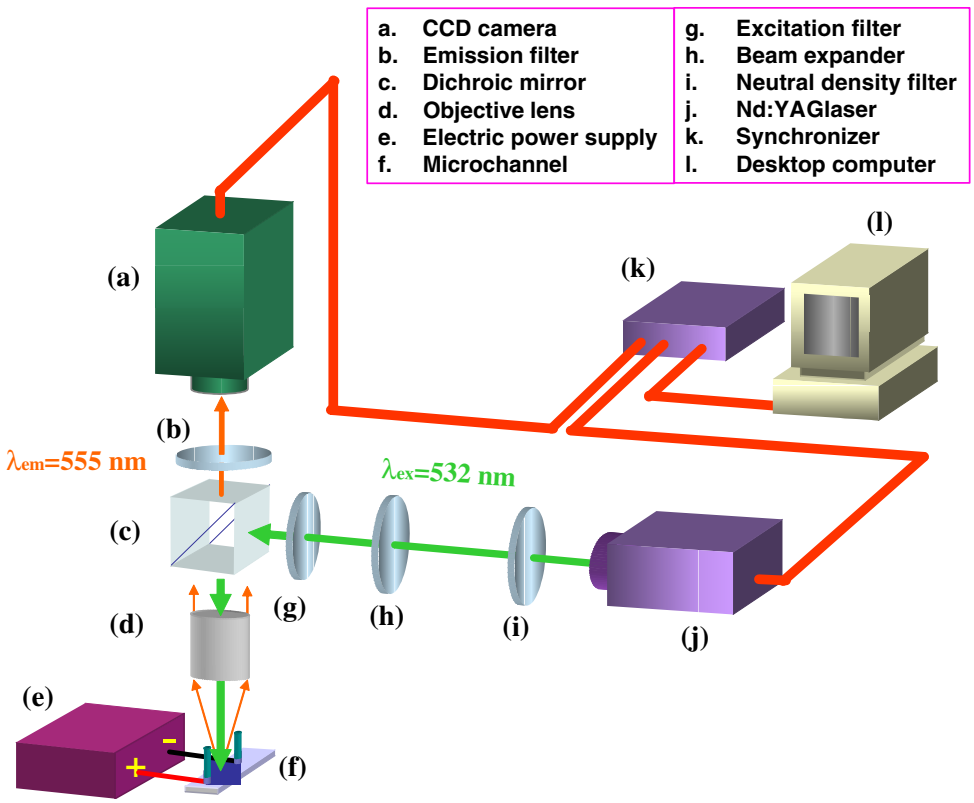


**Fig. 4** Experimental setup for $\mu$PIV technique. The modified carboxyl seeding tracers are excited at 540 nm and emit light at 560 nm. The cooled CCD camera with 1,280 × 1,024 pixels provides 1,280 instantaneous vectors. For a 40× magnification objective lens, the spatial resolution of our $\mu$PIV system is 5.36 × 5.36 μm with a depth of field $\delta z$ = 6.73 μm

in the optical path. Emitted fluorescent signals are then transmitted through an objective lens, dichroic mirror, and emission color filter. Depending on the width of the channel, 20× and 40× magnification objective lenses are chosen for the wide and narrow channels, respectively. The refracted signals are then recorded in an interline cooled CCD camera (PIVCAM13-8, TSI Inc., MN, USA). Images are acquired at 8 frames/s with a resolution of 1,280 × 1,024 video pixels. Finally velocity vector fields are obtained from captured images using a double-frame cross-correlation algorithm. In this study, the interrogation window size is set at 32 × 32 pixels with 50% overlapping.

#### 4.2.1 *Spatial resolution and depth of field of μPIV system*

The theoretical diameter of a diffraction-limited point source of light, obtained from an infinitely corrected optical system, onto a CCD chip is given by

$$d_{diff-\infty} = 2.44 f_{\infty}^{\#} M \lambda_{em} = 1.22\, M\, \lambda_{em} \sqrt{(n/NA)^2 - 1} \tag{6}$$

where $f^{\#}{}_{\infty}$ is $f$-number for infinite-corrected optics, $M$ magnification of the objective lens, $\lambda_{em}$ wavelength of emission light, NA numerical aperture, and $n$ refractive index of the immersion medium. The theoretical diameter of diffraction-limited point source ($d_{diff-\infty}$) identifies the smallest feature an optical system can resolve. For the $\mu$PIV system ($M = 20, n = 1$, NA = 0.4, and $\lambda_{em} = 555$ nm) it has been estimated as $d_{diff-\infty} = 31.31$ μm. The effective particle diameter recorded on the CCD chip is the convolution of the geometric image with the point spread function. If a Gaussian distribution is assumed for both the geometric and diffraction limited images, the effective particle diameter can be given as

$$d_{\text{eff}} = \sqrt{(M d_{\text{P}})^2 + d_{\text{diff}-\infty}^2} \tag{7}$$

where $d_P$ is diameter of particle. The thickness of the measurement plane can be determined as (Meinhart et al. 2000b)

$$\delta z = \frac{3n\lambda_{\text{ex}}}{\text{NA}^2} + \frac{2.16\, n\, d_{\text{P}}}{\text{NA}} + d_{\text{P}} \tag{8}$$

where $\lambda_{ex}$ is excitation wavelength of light in vacuum. Inertial effects of the particles are not significant in this study because the response time of the particles is on the order of $10^{-8}$ s. For an optical magnification of

$M$ = 20, particle diameter of $d_P$ = 500 nm, excitation wavelength of $\lambda_{ex}$ = 532 nm, refractive index of $n$ = 1 and numerical aperture of NA = 0.4, the depth of field is calculated to be 13.18 μm. Since the depth of field ($\delta z$) is larger than channel height ($H$), the $\mu$PIV results presented here are depth-wise averaged values. In this study, the concentration of fluorescent micro-spheres is optimized to have ten particles per interrogation volume $(32 \times 6.7/\mathrm{M})^2 \times \delta z$ μm$^3$ where the system resolution is (32 × 6.7/M). Table 1 lists the above-mentioned important parameters of the $\mu$PIV system. For validation of our $\mu$PIV results, a syringe pump is used to drive a flow in the microchannel at a known flow rate. The error was estimated within 5% for the velocity range studied here (10–1,000 μm/s).

## 4.3 Experimental setup for flows in microchannels

Two kinds of microchannel materials (PDMS–glass and PDMS–PDMS), as well as, two different channel sizes (Channel 1, 300 μm base and Channel 2, 140 μm base) are used to characterize the flow behavior in trapezoidal microchannels. Embedded electrodes are used to apply an electric field along the channel, while a pressure gradient is formed along the channel by creating a pressure head difference between the inlet and exit reservoirs. The applied pressure gradient can be calculated as $\rho_f g \Delta h / L - C_{Loss} \rho_f V_m^2/(2L)$ where $C_{Loss}$ accounts for entrance and exit losses, $\rho_f$ = 998 kg/m$^3$ fluid density, and $L$ = 2 cm channel length. The height difference, $\Delta h$, is varied from 10 to 30 mm. Since $V_m^2/2$ is extremely small compared to $g\Delta h$, the effects of entrance and exit losses are minor in this experiment. In this study, DI water (pH = 7.5) and 100 mM borate buffer (pH = 9.2) are used as the working fluids.

The instantaneous measured velocity field obtained from the $\mu$PIV system can be decomposed into several terms

$$\vec{u}_{measure} = \vec{u}_{flow} + \vec{u}_B + \vec{u}_{PH} \tag{9}$$

where $\vec{u}_{flow}$ is flow velocity, $\vec{u}_B$ velocity contribution due to Brownian motion, and $\vec{u}_{PH}$ electrophoretic velocity. The flow velocity may contain electroosmotic, pressure driven, or mixed electroosmotic-pressure driven component depending on the pumping technique applied along the channel. Detailed discussions of the Brownian velocity ($\vec{u}_B$) and the electrophoretic velocity ($\vec{u}_{PH}$) are presented in the next sections.

### 4.3.1 Elimination of Brownian motion effects

Brownian motion of seeding particles may cause fluctuation of measurement velocities when the size of the particle is less than a few microns. The Brownian motion velocity can be calculated as (Einstein 1956)

$$\vec{u}_B = \sqrt{\frac{2D}{\Delta t}} \vec{e}_r \tag{10}$$

where $\Delta t$ is desired separation time between pulses of laser and $\vec{e}_r$ random unit vector. $D$ is diffusivity of seeding particles, and it can be estimated as (Friedlander 1977)

$$D = \frac{k_B T}{3\pi\mu d_P} \tag{11}$$

Since Brownian motion occurs in all directions, the error due to this random motion can be dramatically reduced by ensemble-averaging techniques if the flow is steady (Meinhart et al. 2000a). Among the three major averaging techniques (average velocity method, average image method, and average correlation method), it was found that the average of correlation functions over 40 experimental runs demonstrated the best result in our particular experiment, and the fluctuation of velocity due to Brownian motion is significantly reduced.

### 4.3.2 Estimation of electrophoretic velocity

Although the seeding particles are neutrally buoyant in both working fluids (DI water and 100 mM borate buffer), they acquire negative charges at pH > 7 due to the presence of a carboxyl group (–COOH) at their surfaces. This causes electrophoretic mobilization of seeding particles when an electric field is applied to drive the flow. The electrophoretic velocity of seeding particles under an applied electric field can be estimated as (Probstein 1984)

**Table 1** Effective particle diameter, measurement uncertainty ($\delta x$), working distance (WD), and depth of measurement for different objective lens used in this study

| $M$ | $n$ | NA | WD (mm) | $f^{\#}{}_{\infty}$ | $d_{diff-\infty}$ (μm) | $d_{eff}$(μm) | $\delta x$ (nm) | $\delta z$ (μm) |
|---|---|---|---|---|---|---|---|---|
| 20 | 1 | 0.40 | 3.0 | 1.1456 | 31.31 | 32.87 | 164 | 13.18 |
| 40 | 1 | 0.60 | 2.5 | 0.6667 | 36.44 | 41.57 | 104 | 6.73 |

Since each particle image is resolved over 3–4 pixels, the experimental uncertainty is estimated as $\delta x \cong d_{eff}/10\,M$

$$\vec{u}_{\mathrm{PH}} = -\frac{ze}{3\pi d_{\mathrm{P}}\mu}\nabla\phi = -M_{\mathrm{PH}}\nabla\phi \tag{12}$$

where $M_{\mathrm{PH}}$ is electrophoretic mobility. In our experimental setup, the electrophoretic mobility of seeding particles can be obtained by subtracting the electroosmotic velocity from the observed flow field. There are two widely used methods to knock out electroosmotic flow: covalent bonding and dynamic coating. Covalent wall coatings can suppress electroosmotic flow in microchip by (a) eliminating the ionizable Si–OH groups on the surface and (b) increasing the viscosity of the coating layer near the surface. However, the protocols used to make covalent coating are both complicated and time consuming. The dynamic coating provides a temporary thin layer of hydrophilic, nonionic polymer on the channel surface using two simple steps. First, the channel surface is rinsed with a coating solution to adsorb a temporary layer of polymer onto the walls. Second, a coating agent such as methyl cellulose or cetyltrimethylammonium bromide is added with the buffer solution.

In this study, the wall surface is dynamically coated with methylcellulose (1.1% w/w MC) to isolate the electrophoretic velocity from the observed velocity. This dynamic coating suppressed 99.5% of electroosmotic flow (Cui et al. 2005). Hence, the error introduced by the electroosmotic mobility (less than 1 μm/s) was not detectable by our μPIV system. It is noteworthy to mention that electrophoresis is a particulate flow phenomenon, so PTV has more physical meaning for the measurement of the electrophoretic velocities of each particle. But, in this study the electrophoretic velocity of the particles is measured by the μPIV detection technique. The PIV detection system provides a mean electrophoretic velocity field rather than distinguishing each particle. However, this approach is more appropriate since the electroosmotic flow field is obtained by subtracting the electrophoretic velocity from the observed velocity field ($\vec{u}_{\mathrm{measure}}$) obtained from μPIV. The mean electrophoretic velocities of the two different buffer solutions (DI water and 100 mM borate buffer) are illustrated in Fig. 5. The direction of the flow in both cases is from cathode to anode, indicated by the negative sign of velocity or mobility (opposite direction of electric field). The electrophoretic mobility in the borate buffer is higher than that of DI water. This is due to the fact that the seeding particles acquire larger negative charges at high pH. The observed velocity is linearly proportional to the applied electric field, and the slope of the curve represents the electrophoretic mobility. However, the linearity of the curve will break down at high electric fields (> 300 V/cm) due to Joule heating effects. Joule heating increases the fluid temperature, which changes the dynamic viscosity and mobility. Note that neither channel materials (PDMS–glass and PDMS–PDMS) nor channel size (300 μm base channel and 140 μm base channel) affects the value of the electrophoretic velocity. In this experiment, electrolysis and resultant bubbles did not affect the magnitude of the observed velocity because we utilized relatively large reservoir compared to the size of the microchannel. The same channel can be used for more than ten times under the high electric field (300 V/cm).

## 5 Discussion of results

### 5.1 Pressure driven flow

In these experiments, the pressure head along the microchannel is generated by changing the height of the liquid column between the inlet and outlet reservoirs. Figure 6 shows the pressure driven velocity profile across the microchannel. Here symbols represent experimental results, while solid lines show the numerical predictions. Numerical results obtained from 3D simulation are also averaged in the depth-wise direction. Simulation results show that the velocity (depth-wise averaged) profile in a rectangular channel is uniform across the channel, except very close to the side wall. However, in a trapezoidal microchannel the average velocity has a tapered-cosine shape. This is due to the fact that in a trapezoidal microchannel side walls are not perpendicular to the base. It is clearly seen that both numerical and experimental results manifest the tapered-cosine velocity profile for the trapezoidal microchannel. The experimental results show good agreement with the numerical prediction except at the tip of the tapered region. This disagreement is primarily due to agglomeration of seeding particles in the corner regions. It was observed that some seeding particles were attached at the corner regions where the PDMS surface roughness was relatively high.

### 5.2 Electroosmotic flow

In electroosmotic flow an external electric field is applied along the channel through electrodes. The embedded electrodes are 1 mm wide, 100 nm thick, and 2 cm apart. Simulation results (not shown here) indicate that this configuration of electrodes provides a uniform electric field along the channel. All experimental data are captured 30 s after initiation of the electric field. The height of the liquid surface is kept at

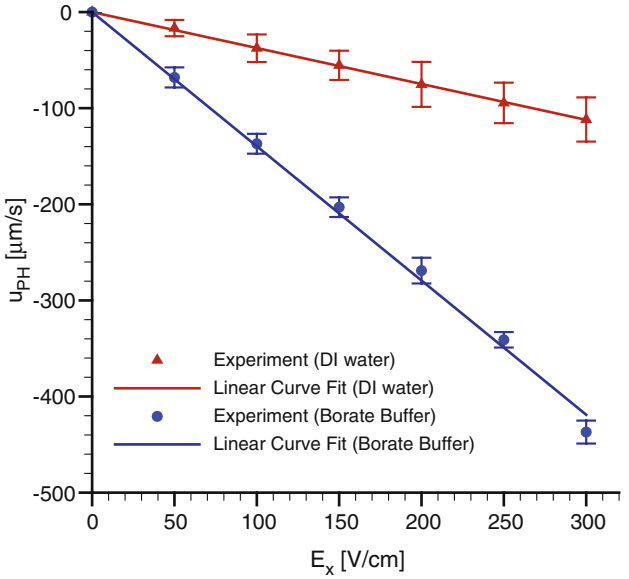


**Fig. 5** Mean electrophoretic velocity of modified carboxyl seeding particles. The estimated mobilities in DI water (pH = 7.5) and 100 mM borate buffer (pH = 9.2) are $-0.3742 \times 10^{-4}$ and $-1.3965 \times 10^{-4}$ cm$^2$/V s, respectively

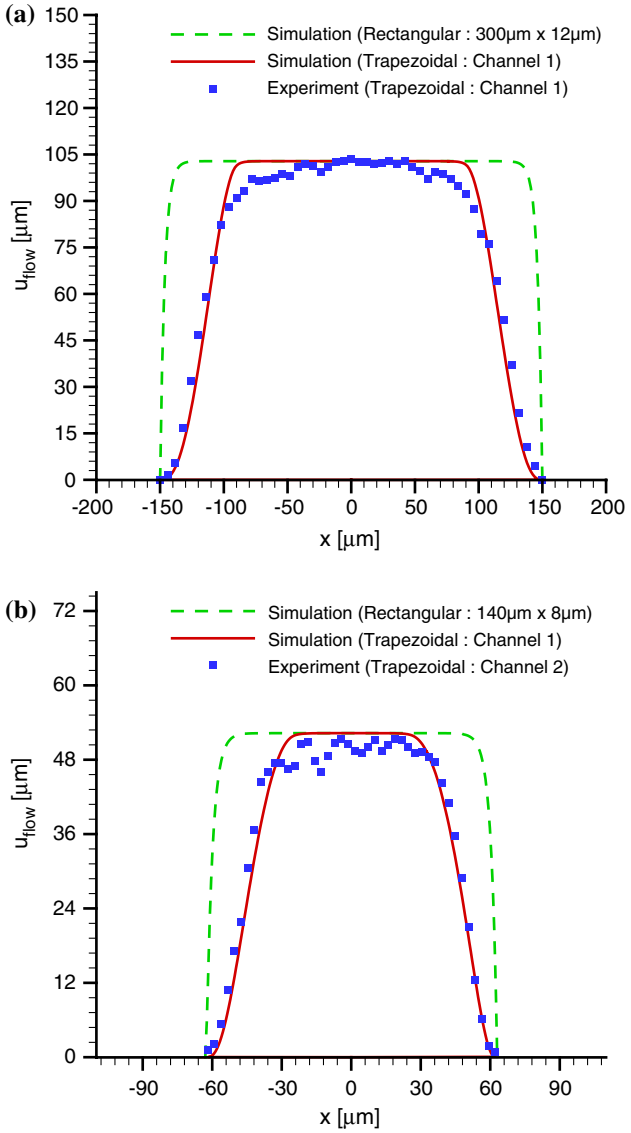


**Fig. 6** Depth-wise averaged velocity profile in pressure driven flow for **a** Channel 1 and **b** Channel 2 presented in Fig. 1 for $dP/dx = -9{,}319$ N/m$^3$. For comparison, numerical results of depth-wise averaged velocity distribution for rectangular microchannels are also presented for the same pressure gradient

the same level to prevent pressure driven flow by fabricating 1 cm diameter inlet and outlet reservoirs.

The electroosmotic velocities for PDMS–glass and PDMS–PDMS are exhibited in Fig. 7 for an electric field range of 50–300 V/mm. Pure electroosmotic flow velocity is calculated by subtracting the estimated electrophoretic velocity ($\vec{u}_{PH}$) from the measured velocity ($\vec{u}_{measure}$) obtained from the $\mu$PIV system. Like the electrophoretic velocity results, the electroosmotic velocity is also a linear function of the electric field. In all cases, the fluid travels toward the cathode, which means that both glass and PDMS surface are negatively charged. Because the electroosmotic flow profile is almost uniform, there was no dependence on channel size or geometries (300 µm base channel and 140 µm base channel). However, experimental results show that the channel material influences the magnitude of electroosmotic flow. If PDMS is used as a channel material, one should take care how the channel surface is treated. In this work plasma was used to bond the top (PDMS) layer and the bottom (PDMS or glass) layer in the fabrication process. Plasma treatment affects the hydrophobicity on both glass and PDMS surfaces. The oxidized PDMS–PDMS channel surface is highly hydrophilic so that relatively high electroosmotic mobility is achieved as shown in Fig. 7. However, the PDMS surface quickly returns to its original hydrophobic character, when the microchannel is flushed three times with a buffer solution. The hydrophobic PDMS is known as native PDMS. The electroosmotic flow is stable in native PDMS for longer periods of time (40 days of observation for this work), even though their mobility values are much smaller. Unlike other studies, no other chemical solutions (such as sodium hydroxide) were loaded into the channel. Hence the surface chemistry prior to the experiment was unaltered. The glass material has substantially higher electroosmotic mobility than the native PDMS. For that reason, the hybrid PDMS–glass channel yields higher electroosmotic velocity than that of native PDMS. This agrees with other researchers' findings (Duffy et al. 1998; Devasenathipathy et al. 2002).

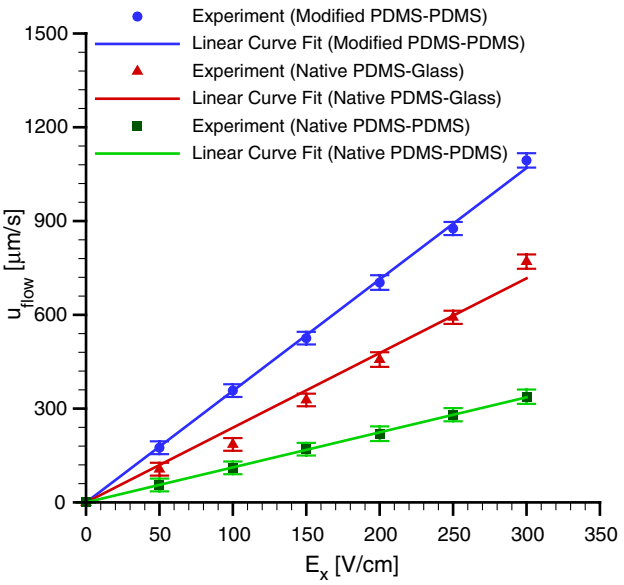


**Fig. 7** Mean electroosmotic velocity of 100 mM borate buffer inside PDMS–glass and PDMS–PDMS microchannels. The estimated mobilities in modified PDMS–PDMS, untreated PDMS–glass, and native PDMS–PDMS channels are $3.5658 \times 10^{-4}$, $2.3890 \times 10^{-4}$, and $1.1202 \times 10^{-4}$ $cm^2/V$ s, respectively

### 5.3 Mixed electroosmotic and pressure driven flow

In this section, the applied electric field is held constant at 100 V/cm and the head difference of the liquid in inlet and outlet capillaries is varied between 10 and 30 mm. Both favorable $(\Delta P/L<0)$ and adverse $(\Delta P/L>0)$ pressure gradient mixed flow cases are studied here. In the case of favorable pressure gradient mixed flow, the flow direction of the pressure driven flow and electroosmotic flow is the same. It may take place in two scenarios. First, if the electric field gets enhanced due to stacking of charged molecules (or seeding particles) on the channel surface, pressure is induced locally. Charged seeding particles may stick to the wall due to geometric complexity or roughness of the channel surface. Second, by maintaining a pumping head along the channel (by connecting the microchannel with a syringe pump or pressure regulator) while an electric field is applied for the purpose of separation or mixing of the species. On the other hand, an adverse pressure gradient arises more often in practice when electroosmotic pumping is desired. Due to the placement of valves or an increase in head of the liquid in the outlet reservoir, the velocity at the center of the channel tends to decrease or even becomes negative (reverse flow). Mixed flow cases are also predicted using the numerical technique presented earlier, and compared with experimental results. It is important to note that the $\mu$PIV system cannot resolve the EDL region. Hence, in the numerical scheme, we have specified the slip velocity boundary conditions on the channel surface, where slip velocity is calculated from electroosmotic mobility and the applied electric field.

Mixed flow under a favorable pressure gradient is illustrated in Fig. 8a. Obviously, as the pressure gradient gets steeper the pressure driven flow becomes more dominant. The tapered cosine profiles are characteristic of pressure driven flow (depth-wise average) velocity profile as discussed in the pressure driven flow section. Experimental data (symbols) match well with numerical predictions (solid lines). The deviation of the profile is the biggest if the flow is pure electroosmotic. The maximum deviation is estimated to be ~9 μm/s. This deviation can be explained from the following facts. In the flow velocity estimation, the mean electrophoretic velocity is subtracted from the observed velocity under the assumption that the seeding particles are distributed uniformly, and they have identical charges and sizes. In practice, each particle experiences slightly different electrophoretic migration. Moreover, since the microchannel is not pretreated with a concentrated sodium hydroxide, there may have been non-uniform zeta potential distribution inside the channel. As compared to pure pressure driven flow (Fig. 6), the mixed velocity (experimental) near the sidewalls is slightly higher than the expected value. This can be attributed to relatively stronger surface interactions (adsorption) between the seeding particles and the channel due to the applied electric field.

Figure 8b demonstrates the combined electroosmotic and adverse pressure driven flow. Although all the values of velocities in this figure are positive, the observed velocity field before subtracting the electrophoretic velocity did indicate reverse flow, especially at the center of the channel. The pure electroosmotic flow is identical to the one in Fig. 8a at an electric field of 100 V/cm. If the pressure driven component were subtracted from the pure electroosmotic flow instead of being added in Fig. 8a, the results would look more like Fig. 8b. This means that Fig. 8a, b are almost symmetric about the horizontal line of pure electroosmotic flow velocity profile. The evidence of linear superposition of electrokinetic (electrophoretic velocity and electroosmotic velocity) and pressure driven flow indicates that the calculation in the PIV post-processing technique, such as ensemble averaging successfully eliminates Brownian motion effects. Mixed flow with an adverse pressure gradient requires careful testing of erroneous vectors if the total flow rate happens to be zero, since ambiguity of the flow

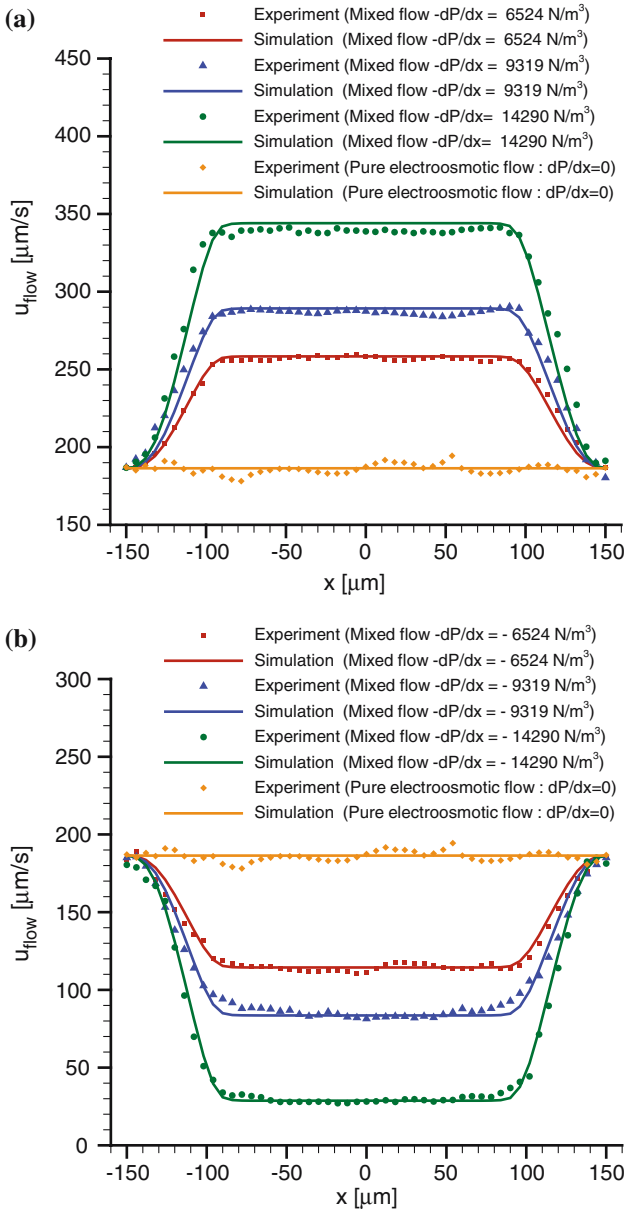


**Fig. 8** Depth-wise averaged velocity distribution in trapezoidal microchannel (Channel 1) for **a** favorable pressure gradient mixed flow and **b** adverse pressure gradient mixed flow. Here experimental results are shown with *symbols* and numerical results with *solid lines*. The applied electric field is kept constant at 100 V/cm, while pressure head is varied

direction sometimes creates errors in the PIV calculation. For this reason, three different magnitudes of pressure gradient were selected so that obvious reverse flow at the center of the channel was observed visually. It turns out that a relatively small pressure gradient can generate reverse flow in our experiment. This implies that the difference in elevation between inlet and outlet is sensitive to generation of pressure head if a micro scale pumping system is interconnected to meso scale devices.

## 6 Summary and conclusions

We have demonstrated pressure, electroosmotic, and mixed electroosmotic-pressure driven flow in a trapezoidal microchannel. A microscale particle velocimetry technique is used to measure the velocity for these conditions. Brownian motion effects are successfully reduced by applying an average correlation function over 40 experimental runs to the PIV measurements. The electrophoretic velocity of modified carboxyl seeding particles is measured to accurately quantify electroosmotic and mixed flows. In electrophoretic mobility measurement, the PDMS channel surfaces are dynamically coated with methylcellulose (1.1% w/w MC) to effectively suppress the electroosmotic flow. Two different buffer solutions (DI water and 100 mM borate buffer) are tested, and it is observed that higher pH value gives higher electrophoretic mobility. The linear relationship between the electric field and the electrophoretic velocity starts to breakdown if the magnitude of the electric field exceeds 300 V/cm.

Three dimensional numerical results of pressure driven flow in a trapezoidal microchannel show a tapered-cosine averaged velocity profile. This unique characteristic of pressure driven velocity profile is experimentally verified by using in-house $\mu$PIV detection technique.

Electroosmotic velocity is obtained by subtracting pre-examined electrophoretic velocity from observed velocity field. Electroosmotic velocity profile is almost uniform and linearly proportional to the electric field regardless of channel dimensions. A modified PDMS surface activated by oxygen plasma enhances electroosmotic flow. Native PDMS, however, is more stable for longer periods of time, though the electroosmotic mobility is very low.

Finally, mixed electroosmotic and pressure driven flow is analyzed. Electroosmotic flow combined with a favorable pressure gradient provides higher pumping capabilities. On the other hand, mixed flow with an adverse pressure gradient showed reverse flow especially at the center of the channel. In both cases, numerical predictions match with experimental data nicely. The maximum deviation of velocity between experiments and predictions was 9 µm/s. Experimental results verify that the observed flow can be decomposed into electrophoretic, electroosmotic, and pressure driven flows after applying an ensemble averaging technique.

**Acknowledgments** The authors thank Mr. Henry Ruff and Mr. Mark Fuller for their valuable suggestions on fabrication techniques. This investigation was supported in part by the Wash-

ington State University Office of Research, and in part by the National Science Foundation under Grant No. CTS0300802.

## References


Bourdon CJ, Olsen MG, Gorby AD (2004) Power-filter technique for modifying depth of correlation in micro-PIV experiments. Exp Fluids 37:263–271

Cui H, Horiuchi K, Dutta P, Ivory CF (2005) Isoelectric focusing in a poly(dimethylsiloxane) microfluidic chip. Anal Chem 77:1303–1309

Cummings EB, Griffiths SK, Nilson RH, Paul PH (2000) Conditions for similitude between the fluid velocity and electric field in electroosmotic flow. Anal Chem 72:2526–2532

Devasenathipathy S, Santiago JG, Takehara K (2002) Particle tracking techniques for electrokinetic microchannel flows. Anal Chem 74:3704–3713

Duffy DC, McDonald C, Schueller OJA, Whitesides GM (1998) Rapid prototyping of microfluidic systems in poly(dimthlsiloxane). Anal Chem 70:4974–4984

Dutta P, Beskok A (2001) Analytical solution of combined electroosmotic/pressure driven flows in two-dimensional straight channels: finite Debye layer effects. Anal Chem 73:1979–1986

Dutta D, Leighton DT (2001) Dispersion reduction in pressure-driven flow through microetched channels. Anal Chem 73:504–513

Dutta P, Beskok A, Warburton TC (2002) Electroosmotic flow control in complex microgeometries. J Microelectromech Syst 11:36–44

Ebadian MA, Dong ZF (1998) Forced convection, internal flow in ducts. In: Rohsenow WM, Harnett JP, Cho YI (eds) Handbook of heat transfer, 3rd edn. McGraw-Hill, New York

Einstein A (1956) Investigations on the theory of the Brownian movement: edited with notes by Fürth R, translated by Cowper AD. Dover, New York

Erickson D, Sinton D, Li DQ (2003) Joule heating and hear transfer in poly(dimethylsiloxane) microfluidic systems. Lab Chip 3:141–149

Friedlander SK (1977) Smoke, dust and haze. Wiley, New York

Hlushkou D, Seidel-Morgenstern A, Tallarek, U (2005) Numerical analysis of electroosmotic flow in dense regular and random arrays of impermeable, non-conducting spheres. Langmuir 21:6097–6112

Keane RD, Adrian RJ, Jensen OS (1995) Super-resolution particle image velocimetry. Meas Sci Technol 6:754–768

Kim MJ, Beskok A, Kihm KD (2002) Electroosmosis-driven micro-channel flows: a comparative study of microscopic particle image velocimetry measurements and numerical simulations. Exp Fluids 33:170–180

Maynes D, Webb AR (2002) Velocity profile characterization in sub-millimeter diameter tubes using molecular tagging velocimetry. Exp Fluids 32:3–15

Meinhart CD, Wereley ST, Santiago JG (1999) PIV measurements of a microchannel flow. Exp Fluids 27:414–419

Meinhart CD, Wereley ST, Santiago JG (2000a) A PIV algolithm for estimating time-averaged velocity fields. J Fluids Eng 122:285–289

Meinhart CD, Wereley ST, Gray MHB (2000b) Volume illumination for two-dimensional particle image velocimetry. Meas Sci Technol 11:809–814

Olsen MG, Adrian RJ (2000) Out-of-focus effects on particle image visibility and correlation in microscopic particle image velocimetry. Exp Fluids 7:S166-S174

Patankar SV (1980) Numerical heat transfer and fluid flow. Hemisphere, New York

Patankar NA, Hu HH (1998) Numerical simulation of electroosmotic flow. Anal Chem 70:1870–1881

Paul PH, Garguilo MG, Rakestraw DJ (1998) Imaging of pressure and electrokinetically driven flows through open capillaries. Anal Chem 70:2459–2467

Probstein RF (1994) Physiochemical hydrodynamics, 2nd edn. Wiley, New York

Santiago JG, Wereley ST, Meinhart CD, Beebe DJ, Adrian RJ (1998) A particle image velocimetry system for microfluidics. Exp Fluids 25:316–319

Sinton D, Erickson D, Li D (2003) Microbubble lensing-induced photobleaching with application to microflow visualization. Exp Fluids 35:178–187

Takehara K, Adrian RJ, Etoh GT, Christensen KT (2000) A Kalman tracker for super-resolution PIV. Exp Fluids 29:SO34-SO41

Tieu AK, Mackenzie MR, Li EB (1995) Measurements in microscopic flow with a solid-state LDA. Exp Fluids 19:293–294

Wereley ST, Gui L, Meinhart CD (2002) Advanced algorithms for microscale particle image velocimetry. AIAA Stud J 40:1047–1055

Xia Y, Whitesides GM (1998) Soft lithograogy. Angew Chem Int Ed Engl 37:550–575

Yang C, Li D (1998) Analysis of electrokinetic flow on the liquid flows in rectangular microchannels. J Colloids Surf 143:339–353